

Research Article

Improving the Spatial Resolution of Bidirectional Cartesian MPI Data using Fourier Techniques

Franziska Werner^{a,b,*} · Nadine Gdaniec^{a,b} · Tobias Knopp^{a,b}

^aSection for Biomedical Imaging, University Medical Center Hamburg-Eppendorf, Germany

^bInstitute for Biomedical Imaging, University of Technology Hamburg, Germany

*Corresponding author, email: f.werner@uke.de

Received 25 November 2016; Accepted 17 February 2017; Published online 23 March 2017

© 2017 Werner; licensee Infinite Science Publishing GmbH

This is an Open Access article distributed under the terms of the Creative Commons Attribution License (<http://creativecommons.org/licenses/by/4.0>), which permits unrestricted use, distribution, and reproduction in any medium, provided the original work is properly cited.

Abstract

Magnetic Particle Imaging (MPI) determines the distribution of superparamagnetic nanoparticles. Signal encoding is achieved by moving a field-free point (FFP) through the volume of interest. Due to its simplicity the Cartesian trajectory is used in many experimental scanner setups. One drawback of the Cartesian trajectory is that the spatial resolution is anisotropic and in particular lower in the orthogonal excitation direction. In order to get fully isotropic resolution one can extend the unidirectional Cartesian trajectory to a bidirectional Cartesian trajectory that switches the excitation direction after a first pass over the volume of interest. When reconstructing each of the unidirectional datasets using e.g. an analytical x -space approach, one obtains two images each having a higher spatial resolution in the excitation direction. Within this work, we introduce a postprocessing method that combines both images and calculates a combined image with fully isotropic spatial resolution.

1. Introduction

Magnetic Particle Imaging (MPI) enables the visualization of superparamagnetic iron oxide nanoparticles (SPIOs) [1]. SPIOs are excited by an externally applied magnetic drive field (DF). Due to the non-linear particle magnetization the recorded spectrum contains higher harmonics that can be used for image reconstruction [2]. Spatial encoding is achieved by applying an additional static magnetic gradient field (selection field), whose field strength is zero at a particular point called the field-free point (FFP). By moving the FFP through space a predefined field-of-view (FOV) can be sampled.

The path of the FFP is usually referred to as the sampling trajectory. The achieved image quality and sampling efficiency are both influenced by the trajectory

type. A comparison of five different trajectories [3] in a simulation study reveals that the Lissajous and the bidirectional Cartesian trajectory provide the best image quality at similar repetition times. In practice, most often Lissajous type trajectories [4] and unidirectional Cartesian trajectories [5] are realized in experimental scanner setups. A first bidirectional scanner has been reported in [6].

The primary advantage of the bidirectional Cartesian trajectory over the unidirectional Cartesian trajectory is to be found in the isotropic spatial resolution, which is provided by the former one, while the latter suffers from a reduced spatial resolution in the orthogonal direction to the fast FFP movement. This can be explained by the nature of the MPI convolution kernel that is significantly sharper in the direction of the FFP movement than in the orthogonal direction. In [5] a fac-

tor of 2.3 for the kernel anisotropy has been reported.

In the trajectory comparison done in [3] the data of the entire trajectories has been used to perform a joint reconstruction. While this is feasible for small FOV it is of great computational effort for large sampling areas. In contrast thereto, the unidirectional sampling trajectory allows reconstructing data line by line and combining these in a postprocessing step. The image reconstruction is thus reduced to a 1D problem, which is significantly easier to handle. In [7] and [8] analytical reconstruction techniques for 1D imaging were developed that either handle the data in Fourier space or in time space. The mathematical equivalence of both methods has been shown in [9]. The time space methods are usually referred to as x -space reconstruction techniques and are very popular in various research works [10–12].

When applying 1D reconstruction to bidirectional Cartesian data one obtains two images both having anisotropic spatial resolution in the orthogonal direction. Within this work we present a method to combine both images to obtain a single isotropic high resolution image. In [6] a very simple image combination has been proposed that adds both images and applies a 'dehazing' filter. We will derive an algorithm that is mathematically exact in case of a known resolution anisotropy.

II. Material and Methods

In this work, we consider two unidirectional datasets with orthogonal excitation directions (x - and y -direction). After reconstruction two 2D images are generated, \mathbf{c}_x and \mathbf{c}_y , with the indices denoting the respective excitation direction. Due to the anisotropic FFP convolution kernel, the image \mathbf{c}_x is blurred along the y -direction and \mathbf{c}_y is blurred along the x -direction. Fig. 1 shows exemplary data that will be used throughout this work. It should be noted that \mathbf{c}_x and \mathbf{c}_y may be reconstructed using analytical techniques (e.g. x -space reconstruction) or algebraic reconstruction techniques [13]. The unidirectional Cartesian data may be reconstructed line by line or by a joint reconstruction approach [14].

From an image processing perspective we can model the anisotropic spatial resolution within the images \mathbf{c}_x and \mathbf{c}_y as a convolution of an isotropic resolution image \mathbf{c} with kernels \mathbf{K}_x and \mathbf{K}_y :

$$\mathbf{c}_x = \mathbf{c} * \mathbf{K}_x, \quad (1)$$

$$\mathbf{c}_y = \mathbf{c} * \mathbf{K}_y. \quad (2)$$

The point spread functions (PSF) \mathbf{K}_x and \mathbf{K}_y describe the response of an imaging system to a point source. It is highly important to note that \mathbf{K}_x and \mathbf{K}_y are not the same as the FFP convolution kernel that is used during the image reconstruction with a Chebyshev or x -

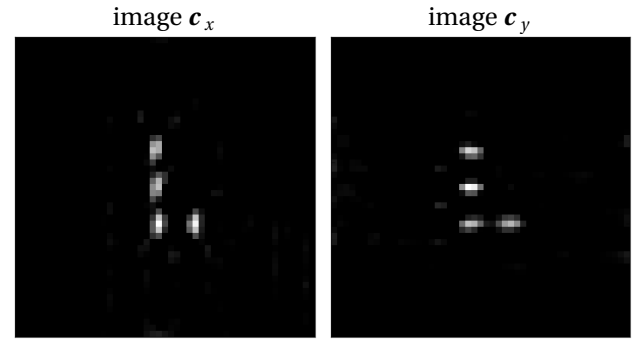


Figure 1: Reconstruction results of two unidirectional Cartesian sampling trajectories with excitation in the x - (left) and in the y -direction (right).

space approach. The images \mathbf{c}_x and \mathbf{c}_y are already corrected for the convolution with the FFP kernel by an appropriate deconvolution during image reconstruction. Alternatively in algebraic reconstruction techniques Tikhonov regularization is used in order to obtain a stable approximate solution and to avoid overfitting.

Using the findings derived from the exemplary MPI data shown in Fig. 1 we can specify the convolution kernels \mathbf{K}_x and \mathbf{K}_y in more detail. In direction of the fast FFP movement the kernels will be a Dirac delta since it will not be possible to increase the spatial resolution in that direction further. In a discrete setting the kernels are thus exactly one pixel wide with a box like characteristic. In the orthogonal direction the blurring can be modeled by several different approaches. The convolution kernel strongly depends on the choice of reconstruction parameters and thus, has to be adapted for different sets of acquisition and reconstruction parameters. Within this work we consider a Hann window

$$H(n) = \frac{1}{2} \left(1 - \cos \left(2\pi \frac{n}{N-1} \right) \right), \quad n = 0, \dots, N-1. \quad (3)$$

The entries $\mathbf{K}_x(l, j)$ with $l = 0, \dots, L-1$ and $j = 0, \dots, L-1$ are thus given by

$$\mathbf{K}_x(l, j) = \begin{cases} H(l - \lfloor \frac{l}{2} \rfloor + \lfloor \frac{N}{2} \rfloor) & , \text{ if } |l - \lfloor \frac{l}{2} \rfloor| < \lfloor \frac{N}{2} \rfloor \\ & \wedge j = \lfloor \frac{l}{2} \rfloor \\ 0 & , \text{ otherwise.} \end{cases} \quad (4)$$

The floored rounding to an integer is defined by $\lfloor \cdot \rfloor$ and L is the number of line scans. The kernel \mathbf{K}_y is then defined by $\mathbf{K}_y = \mathbf{K}_x^T$. The width of the kernel was empirically determined and found to fit best for $N = 7$. Both kernels are shown in Fig. 2.

The goal of this work is to combine \mathbf{c}_x and \mathbf{c}_y in a way that the isotropic image \mathbf{c} is restored. Based on Eq. (1) and Eq. (2) an applied deconvolution to either \mathbf{c}_x or \mathbf{c}_y may be supposed to be the way to go, but a significant increase in noise would be the consequence. Our proposed method avoids this noise amplification.

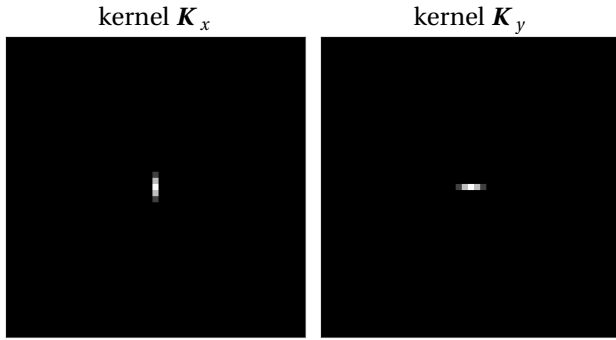


Figure 2: Convolution kernels K_x and K_y that are used in this work to model the anisotropic resolution of unidirectional Cartesian MPI trajectories.

Using the Fourier convolution theorem Eq. (1) and Eq. (2) can be written in Fourier space as multiplications

$$\hat{c}_x = \hat{c} \odot \hat{K}_x, \quad (5)$$

$$\hat{c}_y = \hat{c} \odot \hat{K}_y, \quad (6)$$

where \odot denotes the element-wise multiplication of two matrices. For most kernels a closed form solution of the Fourier transform will be available. In Fig. 3 the Fourier transforms of the images and convolution kernels of the exemplary MPI data are shown. As can be seen the Fourier transforms \hat{c}_x and \hat{c}_y cover a rectangular area in Fourier space with the short axis indicating reduced spatial resolution in this direction. The rectangular shape can be explained by the weighting of \hat{c}_x and \hat{c}_y with \hat{K}_x and \hat{K}_y in Eq. (5) and Eq. (6). For low values within \hat{K}_x or \hat{K}_y it is not possible to retrieve \hat{c} at these frequencies due to noise amplification.

However, since the areas covered by \hat{c}_x and \hat{c}_y in Fourier space are different it is possible to take the best from both datasets to fill a larger area in Fourier space. There are different ways in combining both datasets, but we will use the most simple one that can be derived by adding Eq. (5) and Eq. (6) yielding

$$\hat{c}_x + \hat{c}_y = \hat{c} \odot (\hat{K}_x + \hat{K}_y). \quad (7)$$

In image space this can be equivalently written as

$$c_x + c_y = c * (K_x + K_y). \quad (8)$$

Fig. 4 shows the combined Fourier transformed images $\hat{c}_{xy} := \hat{c}_x + \hat{c}_y$ and the corresponding combined Fourier transformed kernels $\hat{K}_{xy} := \hat{K}_x + \hat{K}_y$. Our proposal is to use Eq. (7) and apply a deconvolution to determine c from given \hat{c}_{xy} and \hat{K}_{xy} . The ill-posedness of the deconvolution is highly reduced since the combined kernel \hat{K}_{xy} has only few areas in Fourier space that are small. In this work we use a simple approach that reformulates Eq. (7) as

$$\hat{c} = \hat{c}_{xy} \oslash \hat{K}_{xy}, \quad (9)$$

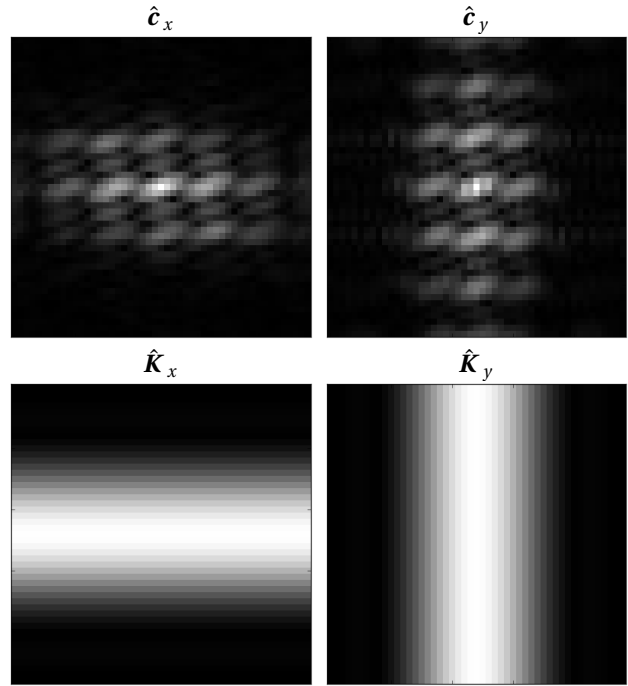


Figure 3: Fourier transforms of the MPI images c_x and c_y and the convolution kernels K_x and K_y .

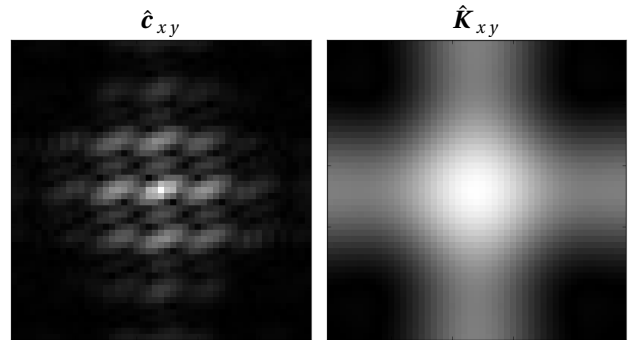


Figure 4: Combination of the Fourier transformed images \hat{c}_x and \hat{c}_y to \hat{c}_{xy} and corresponding combined Fourier transformed kernel \hat{K}_{xy} .

where \oslash denotes the element-wise division of two matrices. Since \hat{K}_{xy} still has some areas with small values we define a mask m that takes a value of 1 where \hat{K}_{xy} has values larger than 10% of its maximum and 0 otherwise. This approach is also known as pseudoinverse filtering. Our final reconstruction formula reads

$$\hat{c}_{xy}^{\text{deconv}} = \hat{c}_{xy} \oslash m \oslash (\hat{K}_{xy} \oslash m + (1 - m)). \quad (10)$$

Fig. 5 shows the mask m and the reconstructed Fourier coefficients $\hat{c}_{xy}^{\text{deconv}}$ for the considered MPI data determined by evaluating Eq. (10).

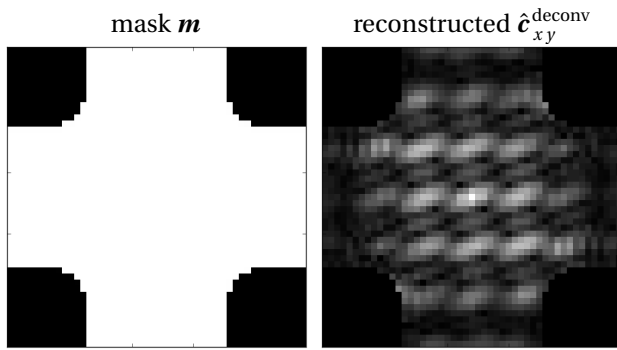


Figure 5: Left: Mask m used to prevent noise amplification due to small values in the combined Fourier transformed convolution kernel \hat{K}_{xy} . Right: Reconstructed Fourier transform $\hat{c}_{xy}^{\text{deconv}}$.

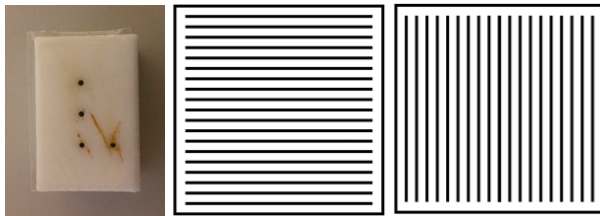


Figure 6: Measurement phantom (left) and discrete sampling schemes for the Cartesian trajectories with fast FFP movement in the x -direction (middle) and in the y -direction (right).

III. Experiments

The measurements were carried out using a preclinical MPI scanner (Bruker Biospin, Ettlingen). The measured phantom was a teflon cuboid of size $30 \times 20 \times 20 \text{ mm}^3$ with four holes arranged like an L (Fig. 6, left). Each hole had a diameter of 1 mm and a depth of 15 mm and was filled with a SPIO-tracer (Resovist, I'rom Pharmaceuticals, Tokio, Japan) with a concentration of $500 \text{ mmol(Fe)L}^{-1}$. In our scan protocol (Fig. 6, middle and left) we performed $L = 49$ onedimensional line scans with the scan line being shifted by a certain increment ($\Delta_{\text{shift}} = 1 \text{ mm}$) after each scan. The amplitude $A = 14 \text{ mT}$ and the gradient $G = 0.75 \text{ T/m}$ led to a scan line of 37.3 mm length in the excitation direction. For shifting the scan line orthogonal to the excitation direction we used the so-called focus field [15, 16]. Afterwards, the excitation and the focus-field direction were exchanged in order to acquire another $L = 49$ line scans in the orthogonal direction. We performed a joint reconstruction to obtain the two Cartesian images, each excited in one dimension, and the bidirectional Cartesian image. Along the scan lines the data are reconstructed on a grid with 49 pixels such that the resulting images are of size 49×49 with an isotropic pixel resolution of $1 \times 1 \text{ mm}^2$.

Image reconstruction was done in this work by the algebraic approach. A system matrix is required for this approach. Therefore, a small delta sample is shifted through the FOV to determine the system matrix for the individual line scans. The resulting linear system is solved by minimizing a first order Tikhonov functional using the iterative Kaczmarz algorithm with two iterations and a manually tuned regularization parameter.

IV. Results

The first row of Fig. 7 shows the results of a deconvolution applied to either c_x or c_y , whereas the second row presents the deconvolution result of the combined image \hat{c}_{xy} and the result of the joint reconstruction c_{xy}^{joint} , where all scan lines of the bidirectional dataset are included in one linear system of equations. It should be noted that, in order to ensure a fair comparison between c_x^{deconv} , c_y^{deconv} , and c_{xy}^{deconv} , we also used corresponding masks for generating c_x^{deconv} and c_y^{deconv} as described in Sec. II for generating c_{xy}^{deconv} . Fig. 7 shows an improvement in spatial resolution in the images c_x^{deconv} and c_y^{deconv} compared to c_x and c_y , but both images suffer from noise amplification along the orthogonal FFP direction. This is not surprising since the unidirectional kernels \hat{K}_x and \hat{K}_y have small values towards marginal areas of their short axis, which raises the noise. In contrast, c_{xy}^{deconv} shows improved spatial resolution with high SNR at the same time.

Fig. 8 gives a detailed impression of spatial resolution and noise. Shown are normalized profiles through the images c_x , c_y , c_x^{deconv} , c_y^{deconv} , c_{xy}^{deconv} , and c_{xy}^{joint} . The four upper plots show profiles through the vertically aligned particle samples. The full width at half maximum (FWHM) for c_x is 3.2 mm, whereas the FWHM for c_x^{deconv} is 2.6 mm. This confirms the visual impression of the spatial resolution being improved by deconvolution. However, the gain in resolution stands against a rise of noise. The third plot shows the profile through the combined deconvolved image c_{xy}^{deconv} . The FWHM with 1.7 mm reveals best resolution for c_{xy}^{deconv} . Furthermore, the noise level is low and comparable to c_x . Same observations can be made for the profiles through the two horizontally aligned point probes that are shown in the four lower plots of Fig. 8. If we now compare c_{xy}^{deconv} with the result of the joint reconstruction c_{xy}^{joint} , both images look similar concerning the spatial resolution, but the SNR with a value of 52 is higher for the combined deconvolved image than the SNR of 25 for the joint reconstruction.

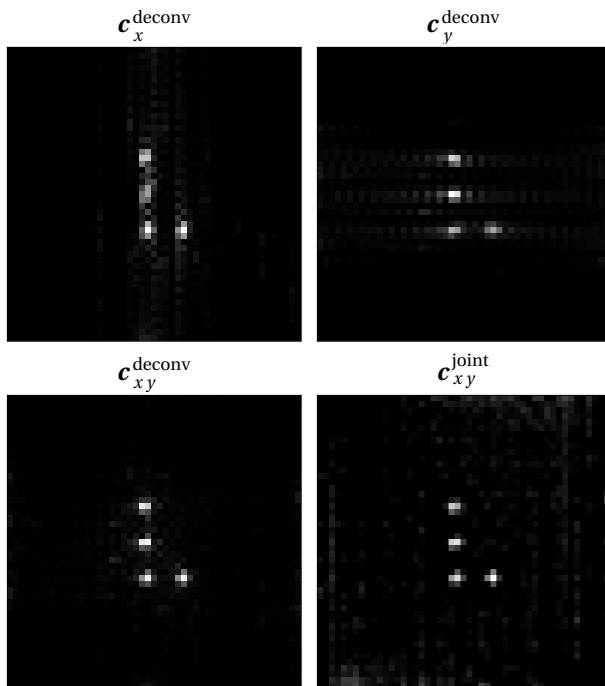


Figure 7: Resulting images after deconvolution applied to either c_x (upper left) or c_y (upper right), the deconvolution result of the combined image c_{xy}^{deconv} (lower left), and the joint reconstruction result c_{xy}^{joint} (lower right).

V. Discussion

In this study we proposed a method to improve the spatial resolution of bidirectional Cartesian MPI data using Fourier techniques. It was shown that in Fourier space the information of both unidirectionally reconstructed datasets can be combined to obtain an image of isotropic spatial resolution. We compared the result with the joint reconstruction approach and showed that both techniques perform similarly concerning spatial resolution. Regarding the noise the joint reconstruction is worse by a factor of two.

Within this work we used a joint reconstruction approach [14] for the reconstruction of the unidirectional MPI scans that leads to less 'hazing' artifacts as has been reported in [6] for separate scan line reconstruction. Therefore our kernel for modeling the resolution loss in the orthogonal direction was chosen to be a short Hann window with seven pixels in length. When using separately reconstructed data it will be necessary to model the 'hazing' effect which is due to the long tail of the FFP PSF in the orthogonal direction to the excitation direction.

The image combination algorithm proposed in this work was applied to 2D imaging using bidirectional imaging trajectories. For 3D imaging it is possible to use tridirectional trajectories consisting of Cartesian sampling with fast FFP movement in x -, y -, and z -direction.

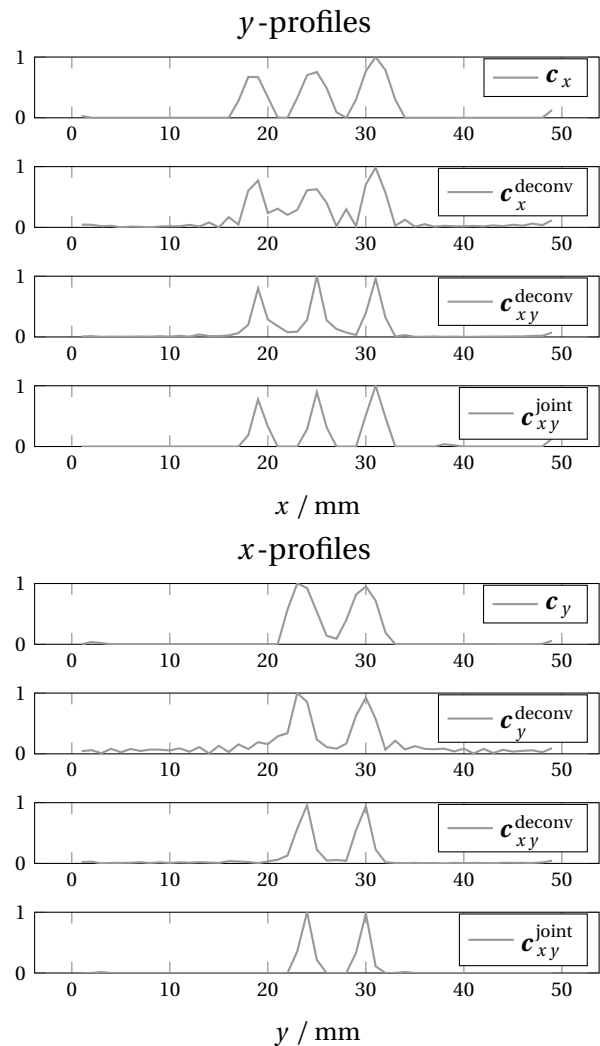


Figure 8: Profiles of the images shown in Fig. 7 through the three particle dots in vertical direction (upper) and through the two dots in horizontal direction (lower). Shown are the datasets c_x , c_y , c_x^{deconv} , c_y^{deconv} , c_{xy}^{deconv} , and c_{xy}^{joint} .

It will be straight forward to apply the image combination method proposed in this work to the 3D case by using kernels being sharp along the excitation direction and broad within the orthogonal imaging plane. The applied Fourier techniques can be applied in the same way to 3D data as for 2D data considered in this work.

Acknowledgment

The authors thankfully acknowledge the financial support by the German Research Foundation (DFG, grant numbers KN 1108/2-1 and AD 125/5-1).

References

- [1] B. Gleich and J. Weizenecker. Tomographic imaging using the nonlinear response of magnetic particles. *Nature*, 435(7046): 1214–1217, 2005. doi:[10.1038/nature03808](https://doi.org/10.1038/nature03808).
- [2] T. Knopp and T. M. Buzug. *Magnetic Particle Imaging: An Introduction to Imaging Principles and Scanner Instrumentation*. Springer, Berlin/Heidelberg, 2012. doi:[10.1007/978-3-642-04199-0](https://doi.org/10.1007/978-3-642-04199-0).
- [3] T. Knopp, S. Biederer, T. Sattel, J. Weizenecker, B. Gleich, J. Borgert, and T. M. Buzug. Trajectory analysis for magnetic particle imaging. *Phys. Med. Biol.*, 54(2):385–397, 2009. doi:[10.1088/0031-9155/54/2/014](https://doi.org/10.1088/0031-9155/54/2/014).
- [4] B. Gleich, J. Weizenecker, and J. Borgert. Experimental results on fast 2D-encoded magnetic particle imaging. *Phys. Med. Biol.*, 53(6):N81–N84, 2008. doi:[10.1088/0031-9155/53/6/N01](https://doi.org/10.1088/0031-9155/53/6/N01).
- [5] P. W. Goodwill and S. M. Conolly. Multidimensional X-Space Magnetic Particle Imaging. *IEEE Trans. Med. Imag.*, 30(9):1581–1590, 2011.
- [6] K. Lu, P. Goodwill, B. Zheng, and S. Conolly. Reshaping the 2D MPI PSF to be isotropic and sharp using vector acquisition and equalization. In *International Workshop on Magnetic Particle Imaging*, 2015. doi:[10.1109/IWMPI.2015.7106994](https://doi.org/10.1109/IWMPI.2015.7106994).
- [7] J. Rahmer, J. Weizenecker, B. Gleich, and J. Borgert. Signal encoding in magnetic particle imaging: properties of the system function. *BMC Medical Imaging*, 9(4), 2009. doi:[10.1186/1471-2342-9-4](https://doi.org/10.1186/1471-2342-9-4).
- [8] P. W. Goodwill and S. M. Conolly. The x-Space Formulation of the Magnetic Particle Imaging process: One-Dimensional Signal, Resolution, Bandwidth, SNR, SAR, and Magnetostimulation. *IEEE Trans. Med. Imag.*, 29(11):1851–1859, 2010. doi:[10.1109/TMI.2010.2052284](https://doi.org/10.1109/TMI.2010.2052284).
- [9] M. Grüttner, T. Knopp, J. Franke, M. Heidenreich, J. Rahmer, A. Halkola, C. Kaethner, J. Borgert, and T. M. Buzug. On the formulation of the image reconstruction problem in magnetic particle imaging. *Biomed. Tech. / Biomed. Eng.*, 58(6):583–591, 2013. doi:[10.1515/bmt-2012-0063](https://doi.org/10.1515/bmt-2012-0063).
- [10] J. J. Konkle, P. W. Goodwill, D. W. Hensley, R. D. Orendorff, M. Lustig, and S. M. Conolly. A Convex Formulation for Magnetic Particle Imaging X-Space Reconstruction. *PLOS ONE*, 10(10):e0140137, 2015. doi:[10.1371/journal.pone.0140137](https://doi.org/10.1371/journal.pone.0140137).
- [11] P. Vogel, M. A. Rückert, P. Klauer, W. H. Kullmann, P. M. Jakob, and V. C. Behr. Traveling Wave Magnetic Particle Imaging. *IEEE Trans. Med. Imag.*, 33(2):400–407, 2014. doi:[10.1109/TMI.2013.2285472](https://doi.org/10.1109/TMI.2013.2285472).
- [12] K. Bente, M. Weber, M. Graeser, T. F. Sattel, M. Erbe, and T. M. Buzug. Electronic field free line rotation and relaxation deconvolution in magnetic particle imaging. *IEEE Trans. Med. Imag.*, 34(2):644–651, 2015. doi:[10.1109/TMI.2014.2364891](https://doi.org/10.1109/TMI.2014.2364891).
- [13] T. Knopp, J. Rahmer, T. F. Sattel, S. Biederer, J. Weizenecker, B. Gleich, J. Borgert, and T. M. Buzug. Weighted iterative reconstruction for magnetic particle imaging. *Phys. Med. Biol.*, 55(6):1577–1589, 2010. doi:[10.1088/0031-9155/55/6/003](https://doi.org/10.1088/0031-9155/55/6/003).
- [14] T. Knopp, K. Them, M. Kaul, and N. Gdaniec. Joint reconstruction of non-overlapping magnetic particle imaging focus-field data. *Phys. Med. Biol.*, 60(8):L15–L21, 2015. doi:[10.1088/0031-9155/60/8/L15](https://doi.org/10.1088/0031-9155/60/8/L15).
- [15] B. Gleich, J. Weizenecker, H. Timminger, C. Bontus, I. Schmale, J. Rahmer, J. Schmidt, J. Kanzenbach, and J. Borgert. Fast MPI Demonstrator with Enlarged Field of View. In *Proc. ISMRM*, volume 18, page 218, 2010.
- [16] J. Franke, U. Heinen, H. Lehr, A. Weber, F. Jaspard, W. Ruhm, M. Heidenreich, and V. Schulz. System Characterization of a Highly Integrated Preclinical Hybrid MPI-MRI Scanner. *IEEE Trans. Med. Imag.*, 35(9):1993–2004, 2016. doi:[10.1109/TMI.2016.2542041](https://doi.org/10.1109/TMI.2016.2542041).